

JAAS

Accepted Manuscript



This is an *Accepted Manuscript*, which has been through the Royal Society of Chemistry peer review process and has been accepted for publication.

Accepted Manuscripts are published online shortly after acceptance, before technical editing, formatting and proof reading. Using this free service, authors can make their results available to the community, in citable form, before we publish the edited article. We will replace this *Accepted Manuscript* with the edited and formatted *Advance Article* as soon as it is available.

You can find more information about *Accepted Manuscripts* in the [Information for Authors](#).

Please note that technical editing may introduce minor changes to the text and/or graphics, which may alter content. The journal's standard [Terms & Conditions](#) and the [Ethical guidelines](#) still apply. In no event shall the Royal Society of Chemistry be held responsible for any errors or omissions in this *Accepted Manuscript* or any consequences arising from the use of any information it contains.

Effect of oxygen in sample carrier gas on laser-induced elemental fractionation in U-Th-Pb zircon dating by laser ablation ICP-MS

Jan Košler^{1,2,3}, Simon E. Jackson², Zhaoping Yang² and Richard Wirth⁴

1 Department of Earth Science, University of Bergen, Allegaten 41, Bergen, N-5007, Norway

2 Geological Survey of Canada, Natural Resources Canada, 601 Booth St., Ottawa Ontario, K1A 0E8, Canada

3 Czech Geological Survey, Klárov 3, Prague 1, CZ-118 21, Czech Republic

4 Helmholtz Centre Potsdam, GFZ German Research Centre for Geosciences, 3.3 Telegrafenberg, 14473 Potsdam, Germany

Abstract

Thermal breakdown of zircon during laser ablation sampling for ICP-MS analysis results in decoupling of Si from Zr, and Pb from U+Th following the reaction $\text{ZrSiO}_4(\text{U,Th,Pb}) = \text{ZrO}_2(\text{U,Th}) + \text{SiO}_2(\text{Pb})$. The rate of the laser-induced elemental fractionation can be linked to the concentration of oxygen in the ambient He sample carrier gas. Deposition of ZrO_2 and SiO_2 on the walls of the ablation craters is enhanced by the presence of oxygen during the ablation, and the composition of the deposit is dominated by ZrO_2 . This study shows that even a small amount of oxygen (e.g., 500 ppm) added to the sample carrier gas can shift the U-Pb ages of zircon by as much as 9%, which is well beyond the typical analytical uncertainty of LA-ICP-MS zircon dating. Addition of up to 2,000 ppm oxygen to the sample carrier also increases the instrument sensitivity by as much as 3 times for light elements and ca. 1.5 times for heavy elements. The increase in sensitivity is accompanied by an increase in the U and Th oxide formation, suggesting that the signal enhancement is not related to the concomitant M^+ and MO^+ ion formation, but rather to the improved atomization and ionization capability of the mixed gas ICP. The study shows that maintaining a constant level of O_2 throughout the ablation cell over an analytical session the time of analysis is a pre-requisite to further improvements in the repeatability of U-Pb LA ICP-MS dating of zircon.

1
2
3
4
5
6
7
8
9
10
11
12
13
14
15
16
17
18
19
20
21
22
23
24
25
26
27
28
29
30
31
32
33
34
35
36
37
38
39
40
41
42
43
44
45
46
47
48
49
50
51
52
53
54
55
56
57
58
59
60

Key words: laser ablation ICP-MS, zircon, elemental fractionation, phase separation, oxygen, focused ion beam, TEM

Introduction

Since the first attempts to date accessory minerals by U-Th-Pb laser ablation ICP-MS (LA-ICP-MS) some twenty years ago [1-4], this technique has become increasingly popular in the geological community. The mineral zircon (tetragonal form of ZrSiO_4) is the most commonly studied accessory phase in magmatic, metamorphic and sedimentary rocks [5] because of its widespread abundance, resistance to abrasion and dissolution in natural environments, its ability to quantitatively retain trace elements over geological time and its low initial content of non-radiogenic Pb.

Determination of U, Th and Pb isotopes in zircon by LA-ICP-MS is complicated by the effects of laser-induced elemental fractionation of Pb relative to U and Th, which are affected by variations in the zircon matrix (chemistry, radiation damage, crystallinity and colour), and mass discrimination of isotopes in the ICP-MS. The potential errors in age determination due to these processes can be reduced or eliminated by matrix-matched calibration and a series of mathematical corrections. The uncertainty associated with the correction for laser-induced elemental fractionation typically dominates the uncertainty budget of U-Th-Pb dating by LA-ICP-MS and an inaccurate correction will result in an erroneous age.

It has been demonstrated that phase separation and formation of particles of variable size and composition are the primary cause of laser-induced elemental fractionation [6], and that the element decoupling can be further enhanced by variable aerosol transport and processes in the ICP [7]. Interaction of laser radiation with zircon typically results in thermal breakdown of ZrSiO_4 to ZrO_2 and SiO_2 and formation of aerosol particles with different composition, size and transport properties [8]. As a result of the preferential partitioning of U+Th

1
2
3 and Pb into ZrO₂ and SiO₂ phases, respectively, the decomposition of zircon by
4 transfer of laser heat can efficiently fractionate these geochronologically
5 important trace elements, potentially resulting in erroneous U-Th-Pb ages
6 obtained by LA-ICP-MS dating.
7
8

9
10 Previous studies have linked the degree of laser-induced decoupling of
11 U+Th from Pb in zircon in any analysis to the chemical composition of the zircon
12 matrix [9] and the amount of radiation damage accumulated since the last
13 annealing of the zircon [10]. More recently obtained laser ablation ICP-MS data
14 for a suite of well characterized zircon samples with a range of compositions and
15 accumulated radiation damage [11] suggest that these factors alone cannot
16 explain the observed variations in the rate of laser-induced elemental
17 fractionation; they may, however, affect the kinetics of the phase separation
18 during the thermal breakdown of zircon.
19

20 In this study, we explore the effects of oxygen present in the sample
21 carrier gas on the laser-induced elemental fractionation of Pb and U+Th during
22 LA-ICP-MS analysis of zircon. As a major component of air, oxygen is a
23 ubiquitous contaminant of the He carrier gas used in LA-ICP-MS to transport
24 ablated material from the sample cell to the ICP. In addition to its potential low-
25 level presence as a natural contaminant in the He supply, its most insidious
26 sources are diffusion through, and degassing of, supply tubing and desorption
27 from surfaces. Monitoring of gas background signal intensities for atmospheric
28 gases or polyatomic ions of atmospheric gases (e.g., masses 29 or 56) show that
29 this can be significant for several hours after starting up the instrumentation. If
30 oxygen plays a significant role in controlling the degree of laser-induced
31 Pb/U+Th fractionation, better control of its effects would lead to improved
32 accuracy of U-Th-Pb dating by LA-ICP-MS.
33
34
35
36
37
38
39
40
41
42
43
44
45
46
47
48
49
50

51 **Laser-induced elemental fractionation of Pb and U+Th in zircon**

52

53
54 Laser-induced elemental fractionation in ICP-MS refers to the change of
55 measured signal intensity ratios on the time scale of a single analysis, typically
56 several hundreds to thousands laser pulses, or between analyses. It has been
57
58
59
60

1
2
3 demonstrated that thermal effects of laser radiation are efficient in triggering the
4 breakdown of tetragonal ZrSiO_4 to a mixture of tetragonal, monoclinic and
5 amorphous ZrO_2 and a mixture of amorphous and high-temperature SiO_2 phases
6 [8] at ca. 1680°C [12]. Corresponding thermally-induced reactions were
7 previously described from zircon heating laboratory experiments [13, 14] and
8 natural rocks that underwent a high-temperature event [15]. It has also been
9 shown that the thermal breakdown of zircon is not limited to nano-second laser
10 ablation but has also been observed during femto-second laser ablation of zircon
11 [16]. The crystal lattice parameters of the newly-formed ZrO_2 and SiO_2 phases
12 are suitable for incorporation of U+Th and Pb, respectively, effectively
13 decoupling the radiogenic Pb produced in zircon from its parent elements. The
14 newly-formed ZrO_2 and SiO_2 phases form particles with different size
15 distributions [8] that may be transported to the ICP with different efficiencies
16 and, or, may atomise and ionise at different depths within the ICP, resulting in
17 the observed U+Th and Pb fractionation.

18
19
20 The rate of elemental fractionation during laser ablation of zircon is
21 related to the progress of the zircon decomposition reaction and is proportional
22 to the inner surface area of the ablation crater, and hence to the crater aspect
23 ratio [17, 18]. The rate of laser-induced elemental fractionation is significantly
24 reduced for shallow craters with low aspect ratio during static ablation or when
25 using dynamic ablation (laser raster or line scan) [19, 20]. In addition,
26 femtosecond laser ablation [21, 22] and ablation with short (DUV) laser
27 wavelength [23] were reported to have reduced laser-induced elemental
28 fractionation. The methods used to correct for laser-induced elemental
29 fractionation include calibration relative to an external zircon standard,
30 mathematical corrections of the fractionating signal or a combination of these
31 two techniques. Corrections made by comparison to an external zircon standard
32 are limited by the need to use the same ablation conditions and corresponding
33 ablation intervals for the unknown and reference samples. This type of
34 correction is prone to error caused by differences in the ablation rates between
35 the unknown and reference zircons due to their chemically and structurally
36 different matrices. The mathematical corrections relate the fractionation rate to
37 the crater diameter [24] or extrapolate the fractionation trend to the start of the
38
39
40
41
42
43
44
45
46
47
48
49
50
51
52
53
54
55
56
57
58
59
60

1
2
3 ablation process. The extrapolation can be done independently for each
4 unknown and reference zircon [25] or it can be modeled for the reference
5 zircons and then applied to the unknown samples [26-27]. Jackson [28] and later
6 also Kuhn *et al.* [29] proposed an alternative correction method that makes use
7 of the empirically observed correlation between elemental ratios of Si/Zr and
8 Pb/U.
9

10
11
12
13 When U-Pb and Th-Pb zircon analyses are to be combined, an additional
14 pre-requisite is that U and Th should not be decoupled during the ablation,
15 transport and ionization in the ICP source of the mass spectrometer. The two
16 elements are typically accommodated in the ZrO₂-rich aerosol particles but due
17 to the incomplete atomization of refractory phases (oxide forming species) in the
18 ICP, and because of the temporal variation of the mean particle size during the
19 course of a laser ablation analysis, the U/Th signal ratio can show a significant
20 variation over the time span of a single analysis [30, 7]. This ICP-induced
21 elemental fractionation can be partly compensated for by particle filtering [7], by
22 using femtosecond pulse width [22] and by ablating with shorter (deep UV)
23 wavelength of the laser [23]. Alternatively, sampling a different part of the ICP
24 can also compensate for the ICP-induced elemental fractionation. This can be
25 achieved by changing the plasma RF power, distance between the ICP and the
26 interface or ICP gas flows.
27
28
29
30
31
32
33
34
35
36
37
38
39
40

41 **Effects of molecular gasses in LA-ICP-MS**

42
43
44 The composition of the ambient gas during laser ablation sampling (often
45 referred to as sample carrier gas) can have a significant effect on the results of
46 LA-ICP-MS analysis. In the ablation cell, it impacts on the formation and
47 transport of the ablated aerosol. Downstream from the ablation cell, the sample
48 carrier gas enters the ICP and its composition plays an important role in the
49 atomization and ionization of the sample. The presence of foreign (often
50 molecular) gasses in the sample carrier gas originates from gas impurities,
51 degassing of inner surfaces of the ablation cell and tubing, diffusion of air
52 through the tubing walls, any leaks and ablation of samples that produce gaseous
53
54
55
56
57
58
59
60

1
2
3 species. In a typical LA-ICP-MS experiment, it is often difficult to separate the
4 effects of sample carrier gas during processes that occur at the ablation site and
5 in the ICP but it is practical to discuss the two effects separately.
6
7

8
9
10 *Composition effect of sample carrier gas on the ablation and transport of aerosol*

11 The early laser ablation ICP-MS studies used Ar as the sample carrier gas,
12 presumably because it did not require different settings of the ICP matching
13 network that was tuned for the Ar plasmas and because the superior transport
14 properties of He were not yet recognized. For routine analysis, use of Ar as the
15 sample carrier gas was later replaced by He [17, 31] because its higher thermal
16 conductivity and lower density and viscosity improve sample removal, reduce
17 plasma shielding and result in better overall transport efficiency during ablation
18 at atmospheric pressure. Avoiding the use of Ar as the sample carrier gas also
19 reduces the formation of Ar-based species that in some types of analysis may
20 interfere with the analytes [32].
21
22
23
24
25
26
27

28 In an attempt to control the elemental fractionation of Pb and U, Hirata
29 [33] introduced freon R-134a gas (1,1,1,2-tetrafluoroethane) into the He sample
30 carrier gas to the ablation cell. The freon reacted with U to produce a volatile U
31 fluoride compound (UF_6) under the high temperature conditions at the ablation
32 site, which improved the transmission efficiency for U. In another study, addition
33 of oxygen to the He carrier gas was shown to have a significant effect on
34 elemental fractionation during the ablation of silicate and sulphide samples [34].
35 Concentrations of O_2 in the He sample carrier gas as low as few hundred ppm
36 were sufficient to affect the aerosol properties (possibly due to redox reactions
37 in the plasma plume) and to change the extent of elemental fractionation. An
38 application where this applies is LA-ICP-MS analysis of samples that will not fit
39 in the ablation cell, where ablation in an open transport system is typically used.
40 Sampling is carried out in air [35, 36], which is then exchanged for Ar in a gas
41 converter apparatus and introduced into ICP-MS instruments. The analytical
42 performance of the open transport setup is comparable to a standard closed
43 transport LA-ICP-MS [36].
44
45
46
47
48
49
50
51
52
53
54
55
56
57
58
59
60

Effect of gas composition on the atomization and ionization in the ICP

The effect of ICP gas composition on the analytical performance of the ICP-MS has been a subject of numerous studies (see the overviews in [37-40]). Most of them explored the addition of polyatomic gasses such as nitrogen, hydrogen, oxygen, methane and air, or monoatomic gasses (helium or xenon) to Ar with the aim of improving the atomization and ionization power of the ICP. The foreign gasses were added to all three gas streams of the ICP, often with notable effects on the signal intensity. However, these experiments could often not be reproduced by different instruments in other labs. Enhancement of signal intensity by addition of nitrogen to the ICP has been explained by better thermal conductivity of N₂ compared to Ar [41, 42], which should facilitate the transfer of energy between the gas and sample aerosol within the plasma (thermal conductivity of N₂ at 7,000K is 32x higher compared to Ar, [43]). Addition of N₂ to the Ar ICP also reduces molecular interferences of MO⁺, since the formation of strong bonds in the NO molecules effectively scavenges O⁺ ions present in the ICP [41, 43]. Similar to N₂, the effect of signal enhancement due to improved thermal conductivity was reported for addition of H₂ [40]. In another study, signal enhancement was observed as a result of addition of O₂ to the ICP for the purpose of oxidising carbon during the analysis of organic compounds, and also to limit the deposition of reduced organic material on the sampling cone [44].

Lack of reproducibility of experiments with mixed-gas plasmas, and especially contradicting results for signal enhancement by addition of molecular gases to the Ar ICP have led to limited application of this technique. Difficulties in achieving signal enhancement by addition of foreign gasses to the ICP by some laboratories have been attributed to air entrainment into the ICP [45] that is, when at atmospheric pressure, effectively a mixed-gas plasma (Longerich, pers. com. 2013). Subject to the variable amount of air that is already present in the Ar, the introduction of additional gas may or may not improve the atomization and ionization power of the ICP.

Experimental setup

The instrumental setup used for the laser ablation experiments is shown in Fig. 1. We used a 193 nm ATL excimer laser that was part of an Analyte 193 (Photon Machines Inc.) laser ablation system at the Geological Survey of Canada to ablate the GJ-1 and Mud Tank zircon samples [46, 47]. The laser was fired at a repetition rate of 10 Hz and energy density of 6.4 J/cm² to produce single, 26 μm wide craters in zircon sample GJ-1. The two-volume HelEx sample cell was flushed with a mixture of He and O₂ gases (total 1 l/min) via the gas inlet into the base of the cell. Variable nominal concentrations of oxygen (0-2,000 volume ppm) in the He sample carrier gas were achieved by mixing, up-stream from the ablation cell, pure He (better than 99.999%) with a mixture of He+O₂ (500 ppm) or with pure oxygen to achieve higher O₂ contents (up to 2,000 ppm). The gas flows were controlled using external MKS (model 1479A/246C) and Alicat Scientific (MC series, part of the Analyte 193 laser ablation system) mass flow controllers. The sample carrier gas containing the ablated aerosol was then mixed with Ar (0.9 l/min) in a T-junction (without any signal smoothing device) and introduced into the shielded ICP (RF = 1200 W) of a quadrupole ICP-MS (Agilent 7700x). Signal intensities of ²⁹Si, ⁹⁶Zr, ^{206,207,208}Pb, ²³²Th, ²³⁸U, ²⁴⁸ThO and ²⁵⁴UO were measured in time-resolved mode with respective dwell times of 5, 5, 15, 50, 10, 10 and 10 ms. A typical analysis consisted of data acquisition of a gas blank (30s) followed by a 60s acquisition of laser ablation signal (600 laser pulses).

Data were processed off-line in an MS Excel spreadsheet. The data reduction included correction for gas blank and calculation of the slope and intercept values for the observed fractionation trends [48]. In addition to the mean values of the signal intensity ratios, the slope and the intercept (value of the signal intensity ratio at the start of ablation) were used to characterize the laser-induced elemental fractionation. These were calculated assuming a linear change of the signal intensity ratios with the ablation time (i.e., the number of laser pulses applied to the sample). Prior to the calculation, all time-resolved signal intensity ratios were visually inspected for linearity and lack of excursions that could impact on the calculated results.

1
2
3 In the second part of the study, we used identical experimental
4 parameters, except for firing 1500 laser pulses using a beam diameter of 86 μm ,
5 to ablate and analyze the Mud Tank zircon sample at variable O_2 concentrations
6 in the He sample carrier gas. The Mud Tank zircon, rather than the GJ-1 zircon,
7 was used for this part of the study because it was available to us in greater
8 quantities and larger pieces. The zircon sample was sectioned using a low speed
9 saw and the two perpendicular-cut surfaces of each part of the sample were
10 polished before the zircon grain was re-assembled in the sample holder of the
11 HelEx ablation cell. This formed a flat polished sample surface that was
12 perpendicular (i.e., horizontal) to the incident laser beam with a joint between
13 the two parts of the sample that was parallel to the laser beam (i.e., vertical).
14 This sample arrangement allowed the Mud Tank zircon to be ablated down the
15 joint and, following the ablation, the two parts of the sample to be separated,
16 exposing the cross-section of the ablation pits (Fig. 2).
17

18
19
20
21
22
23
24
25
26
27 The laser pits in one part of the Mud Tank zircon sample were filled with
28 epoxy to form a flat surface that was coated with protective layer of Pt. The wall
29 and bottom parts of the pits were sectioned by focused ion beam (FIB) that uses
30 accelerated beam of Ga ions to sputter material from the target and produces
31 electron-transparent foils (ca. $20 \times 10 \times 0.12 \mu\text{m}$) for subsequent TEM study [49,
32 50, Fig. 2]. The TEM analytical work was carried out at GFZ Potsdam using an
33 FEI Tecnai G2 F20 X-Twin system using a 200 kV electron beam generated from
34 a field emission gun. The TEM study included bright-field and dark-field imaging,
35 high-angle annular dark field (HAADF) and high-resolution transmission
36 electron microscopy (HRTEM) imaging as well as electron diffraction analysis
37 (fast Fourier transform - FFT) and energy dispersive x-ray analysis (EDX). The
38 spatial resolution of the EDX is controlled by the beam diameter, which was ca.
39 1–2 nm.
40
41
42
43
44
45
46
47
48
49
50
51
52
53
54
55
56
57
58
59
60

Results

Effect of oxygen addition on measured signal intensity

Mean signal intensities obtained by LA-ICP-MS analysis of the GJ-1 zircon at different levels of oxygen in the He sample carrier gas are shown in Fig. 3. The data were collected on two different days and using two different experimental setups. During day 1, the oxygen dilution was achieved by addition of He+O₂ mixture to the stream of pure He via a mass flow controller. This arrangement was used to achieve low oxygen concentrations (up to 500 ppm). To achieve higher oxygen concentrations (500 to 2,000 ppm) for the experiments run on day 2, the He+O₂ mixture was replaced by a pure oxygen supply. The data suggest that the instrument sensitivity was somewhat (ca. 30%) lower during the experiment done on day 2 but data from both days show a similar trend. As expected, the addition of oxygen to the He sample carrier gas increased the abundance of oxide ions in the ICP. In this case, an increase from 30 to 14,000 cps and from 450 to 120,000 cps was observed for ²³²ThO⁺ and ²³⁸UO⁺, respectively when oxygen level increased from 0 to 2,000 ppm. At the same time, a signal intensity increase was observed for masses ²⁹Si (2.03 to 6.06 million cps), ⁹⁶Zr (42.4 to 84.7 million cps), ²⁰⁶Pb (3,750 to 6,500 cps), ²³²Th (29,000 to 42,000 cps) and ²³⁸U (600,000 to 916,000 cps). Correspondingly, the oxide formation (MO⁺/M⁺*100) increased from 0.1 to 33% and from 0.08 to 13% for ²³²ThO⁺ and ²³⁸UO⁺, respectively (Fig. 3D). Overall, while the increase in oxide ion abundance with increasing oxygen concentration in the He sample carrier gas was ca. 270-470 fold, the increase in signal intensity for the measured elemental ions varied between 3 and 1.5 fold for the light and heavy elements, respectively, effectively shifting the maximum of the instrument's mass response curve towards lighter masses. The signal intensities of ²³²ThO⁺ and ²³⁸UO⁺ show a linear increase with increasing concentration of oxygen in the He sample carrier gas up to ca. 500 - 1,000 ppm O₂, and it is not accompanied by a complementary decrease of signal of elemental ions as it would be the case if there were a competition between concomitantly produced MO⁺ and M⁺ ions.

Effect of oxygen addition on laser-induced elemental fractionation

The effects of oxygen addition to the He sample carrier gas on laser-induced fractionation of elements are shown in Fig. 4. The mean values of the Si/Zr and Pb/U ratios determined from the ablation of the GJ-1 zircon increase by ca. 9% between 0 and 500 ppm of added oxygen. The 9% increase of $^{206}\text{Pb}/^{238}\text{U}$ can be translated do an age difference of ~60 million years for this sample. The initial rapid increase is followed by a slower rise of the ratios up to 2,000 ppm of added oxygen. In gross terms, the trends of increase in mean values of Si/Zr and Pb/U ratios with increasing amount of added O₂ follow each other. A closer inspection of the fractionation trends shows that in the case of the Si/Zr signal intensity ratios, the change of the mean ratio value with increasing concentration of O₂ is due to the increase of both the slope and the intercept values of the Si/Zr fractionation trend. However, in the case of the Pb/U signal intensity ratios, the change of the mean value can be attributed mainly to the change of the intercept value, while the slope of the fractionation trend remains virtually the same for oxygen concentrations in the He sample carrier gas between 0 and 500 ppm. Since it is usually the mean value of the Pb/U fractionation trend or the value of its intercept (the value of the Pb/U ratio at the start of laser ablation) that are used to calculate the U-Pb ages in laser ablation ICP-MS dating of zircon, either of these two approaches might result in erroneous U-Pb zircon ages when the oxygen concentration in the ablation cell varies between analysis of samples and standards (e.g., during period of significant degassing of tubing, samples and ablation cell surfaces after instrument start up).

Oxygen-induced phase changes during laser ablation of zircon

Secondary electron imaging of the ablation pits produced in the Mud Tank zircon sample at different concentrations of oxygen in the He sample carrier gas shows layers of molten or microcrystalline material deposited on the ablation pit walls, as well as some melt at the bottom of the pits (Fig. 5). The layer deposited on the walls shows corrugated, vertically oriented structures with later cooling cracks that cut across the corrugations. With increasing amount of oxygen in the He carrier gas, the wall deposits show a change from a discontinuous and intensely corrugated deposit at low oxygen concentration to smooth, continuous and more

1
2
3 voluminous layer at higher oxygen concentrations. In contrast to the crater walls,
4 the deposits at the bottom of the pits are smooth, featureless and thinner
5 compared to the deposit on the walls. No visible variation in the structure and
6 composition of the pit bottoms has been observed for different concentrations of
7 oxygen in the He sample carrier gas.
8
9

10
11 High-angle annular dark field (HAADF) images and bright (BF) and dark
12 (DF) field images obtained by TEM from the focused ion beam (FIB) foils cut
13 from the wall and bottom of the pits ablated in the Mud Tank zircon at different
14 concentrations of oxygen in the He sample carrier gas are shown in Fig. 6. The
15 HAADF images suggest that the deposit on the crater walls is mainly made of
16 coarsely crystalline monoclinic ZrO_2 , nanocrystalline ZrO_2 and amorphous SiO_2 .
17 Only a small proportion of the wall deposit is composed of tetragonal $ZrSiO_4$. The
18 interface between the zircon that forms the crater wall and the mixture of ZrO_2
19 and SiO_2 phases in the layer is sharp (cf. the BF and DF images in Fig. 6),
20 suggesting that the phases that constitute the wall layer formed prior to being
21 deposited on the crater walls; i.e., that the ZrO_2 and SiO_2 phases did not form in-
22 situ. The deposit is heterogeneous on the micron and sub-micron scale, with
23 discrete domains formed by different phases. The texture of the layer resembles
24 that of a flowing viscous liquid, suggesting that the material was plastic and
25 perhaps partly molten when the layer formed, and, although its thickness varies
26 within the individual craters, it generally increases with increasing
27 concentrations of oxygen in the He sample carrier gas. In contrast to the deposit
28 on the crater walls, the phase composition revealed by the FIB foils cut from the
29 bottom of the craters is more uniform. A 150-180 nm thick layer of glass, which
30 has a stoichiometric composition of $ZrSiO_4$, covers the bottoms of all the craters.
31 The thickness of the glass layer does not vary with changing concentrations of
32 oxygen in the He sample carrier gas.
33
34
35
36
37
38
39
40
41
42
43
44
45
46
47
48
49
50
51
52
53
54
55
56
57
58
59
60

Discussion

Phase separation during the thermally-induced breakdown of zircon

The phase change of ZrSiO_4 to ZrO_2 and SiO_2 observed in this study as a result of interaction of DUV excimer laser radiation with natural zircon is similar to the laser-induced thermal effects observed by Kosler et al. [8] for zircon ablated by a solid state ns UV Nd:YAG laser ($\lambda=266$ nm), by Wang et al. [51] for IR CO_2 laser ablation and also for UV femtosecond laser ablation of zircon ([16] and the unpublished FIB/TEM data of Kosler and Wirth for zircon ablated by a UV femtosecond laser). The previously published TEM analysis of ablation craters produced by the UV Nd:YAG laser with poor energy beam profile [8] is indicative of an in-situ phase reaction in the crater walls. By contrast, the present study of craters produced with the DUV excimer laser with significantly better beam energy profile shows a sharp interface between the crater walls (ZrSiO_4) and the wall deposit ($\text{ZrO}_2 + \text{SiO}_2 + \text{ZrSiO}_4$), suggesting that the phase reaction took place prior to the deposition. There is also a notable difference between the structure of the crater walls and their bottoms. The surfaces of the crater bottoms are clean with just a thin layer (150-180 nm) of ZrSiO_4 glass while the deposits on the walls contain up to several μm thick layers of coarsely crystalline monoclinic and nanocrystalline ZrO_2 (dominant phase), amorphous SiO_2 and small amounts of tetragonal ZrSiO_4 . This observation points to the phase reaction $\text{ZrSiO}_4 = \text{ZrO}_2 + \text{SiO}_2$ taking place during or after the removal of material from the crater bottom, but prior to, or at the time of, its deposition on the crater wall. It also suggests that the composition of aerosol produced by laser ablation of zircon is already fractionated when it leaves the ablation crater. It should also be noted that formation of ZrSiO_4 melt at the bottom of laser craters would not be expected because zircon melts incongruently or decomposes to ZrO_2 and SiO_2 prior to melting [52], and the amorphous state of the melt is not stable during cooling [53]. The thin layer of ZrSiO_4 glass is likely non-stable and its existence can only be explained by fast quenching between the laser pulses.

The banded structure of the wall deposits, where the SiO_2 -rich layers alternate with the more voluminous ZrO_2 -rich layers (cf. Fig. 6), may form during the deposition as a result of sputtering and re-deposition of material on the

1
2
3 crater walls in combination with small variations in the ablation parameters or
4 after the deposition of the layer by phase separation within the hot and
5 presumably plastic wall deposit. The apparent volume dominance of the ZrO₂
6 phases over the SiO₂ phases in the wall deposit is consistent with the higher
7 condensation temperature of ZrO₂ (4300 °C) compared to SiO₂ (2230 °C) and its
8 preferential condensation closer to the ablation site, and with the observed
9 increase of Si/Zr and also Pb/U ratios during the ablation (positive slopes of the
10 Si/Zr and Pb/U fractionation trends in Fig. 4B and C, respectively). The function
11 of the crater walls as efficient scavengers of the ablated aerosol has been pointed
12 out by previous studies [17, 18] and it is reflected in the commonly used laser
13 ablation sampling strategies that typically aim at the crater aspect
14 (depth/diameter) ratio of less than 1 [20] in order to reduce the laser-induced
15 elemental fractionation. The present study, for the first time, provides data that
16 illustrate in detail the mechanisms of elemental fractionation within the ablation
17 craters, namely the importance of the crater walls during laser ablation of zircon.
18 The element fractionation trends for different concentrations of oxygen in the He
19 sample carrier gas shown in Fig. 4 suggest that the Si/Zr fractionation follows
20 only partly the fractionation of Pb/U, despite the respective compatibilities of Pb
21 and U with the SiO₂ and ZrO₂ phases. This is best shown by a comparison of the
22 intercept and slope values for the ²⁹Si/⁹⁶Zr and ²⁰⁶Pb/²³⁸U fractionation trends at
23 different concentrations of oxygen (cf. Fig. 4). Both the slope (which reflects the
24 fractionation rate) and the intercept (which reflects the mass bias) of the
25 ²⁹Si/⁹⁶Zr fractionation trend change with increasing concentration of oxygen,
26 while for the ²⁰⁶Pb/²³⁸U fractionation, the slope remains virtually constant. It has
27 been proposed [28, 29] that the Si/Zr values may be used to correct for the Pb/U
28 laser-induced elemental fractionation during laser ablation of zircon. Results of
29 this experiment suggest that such correction will only work, provided that there
30 is no ambient oxygen available during laser ablation or when the oxygen
31 concentration remains constant during the analysis. Some of the data in Fig. 4
32 show a shift in the Pb/U intercept values between measurements that were done
33 on two different days, as well as the change in the increase of the value of the
34 intercept with added O₂ to the He sample carrier gas at ca. 500 ppm O₂. These
35
36
37
38
39
40
41
42
43
44
45
46
47
48
49
50
51
52
53
54
55
56
57
58
59
60

1
2
3 changes are interpreted as resulting from variable mass bias between the two
4 days and at high concentrations of O₂ in the ICP.
5
6

7
8 *Sources of oxygen and its effects on laser-induced elemental fractionation*
9

10 Both our SEM and TEM observations suggest that the thickness of the wall layers
11 composed of a mixture of monoclinic and nanocrystalline ZrO₂, amorphous SiO₂
12 and some tetragonal ZrSiO₄ increases with increasing ambient concentration of
13 O₂, which, in turn, positively correlates with the Si/Zr and Pb/U fractionation
14 patterns (cf. Figs 4-6). This leads to the conclusion that the concentration of
15 oxygen in the ablation cell is an important factor that controls the laser-induced
16 elemental fractionation during laser ablation of zircon.
17
18

19 The amount of oxygen that is needed to significantly change the element
20 fractionation rates is fairly small. Our experiment suggests that only 500 ppm O₂
21 in the ablation cell can change the apparent U-Pb age of zircon by as much as 9%
22 which makes the analysis useless for many geological applications. Such low
23 concentrations are easily achievable through impurities in the sample carrier
24 gas, degassing of the inner surfaces of tubing, samples and ablation cell, residual
25 air and moisture present in the ablation cell after it was opened to the
26 atmosphere and potential leaks in the system. The mere presence of oxygen in
27 the ablation cell would not be an obstacle to accurate analysis, provided that it is
28 constant with time and location within the cell so that corresponding data can be
29 obtained from samples and standards. Spatial and temporal variations in oxygen
30 concentration in the ablation cell can, however, result in erroneous U-Pb ages
31 obtained by laser ablation ICP-MS analysis of zircon.
32
33

34 Another potential source of oxygen is the sample itself. Laser ablation of
35 oxides and silicates, such as zircon, will break the atomic bonds in the structure
36 and release oxygen to the sample carrier gas. It has been estimated [34] that a
37 typical ablation crater in silicate glass (60 μm wide and 100 μm deep laser pit in
38 NIST 612) can produce up to 0.6 μg of oxygen. If some of this is present as free
39 oxygen, high concentrations of oxygen may be present at the ablation site, which
40 may significantly alter the elemental fractionation pattern. The amount of
41 oxygen released by ablation of zircon from a crater that is 26 μm in diameter and
42 60 μm deep (such as the ablation craters produced in zircon GJ-1 in this study) is
43
44
45
46
47
48
49
50
51
52
53
54
55
56
57
58
59
60

0.05 μg , which represents a quantity that could significantly affect the laser-induced Pb/U and Pb/Th elemental fractionation, particularly if there is a progressive increase in oxygen concentration in the pit as it deepens by ablation. Accordingly, it is important that the matrices of samples and standards are identical (or at least very similar) in their composition and oxygen content. This may be difficult to achieve for natural samples that typically have a range of compositions and are rarely homogeneous. In case of the mineral zircon, an additional complexity comes from its variable ages and U (Th) contents that lead to variable degree of radiation damage (metamictization). Allen and Campbell [10] and Kooijman et al. [11] have recently reported on the effects of radiation damage in zircon on the accuracy of U-Pb zircon ages obtained by laser ablation ICP-MS. While the former study concluded that the effects were systematic (there was a correlation between the calculated radiation damage and bias of the U-Pb age), the data presented in the latter study show no such correlation. Given that metamictization of zircon by radiation damage typically leads to an increase of oxygen content in its structure [54], laser ablation of zircons with variable degree of radiation damage can liberate different amounts of oxygen that can affect the elemental fractionation patterns to a different degree. The relation between radiation damage, variable amount of oxygen that is prone to liberation during the ablation of variably metamict zircons and fractionation pattern of Pb/U (and also Si/Zr) may explain the apparent discrepancy in conclusions of the two aforementioned studies [10 and 11].

Oxygen effects on ICP-MS signal enhancement

The observed enhancement of instrument sensitivity by as much as 3 times due to addition of small amount of oxygen to the He sample carrier gas was accompanied by an increase in oxide signal intensity by as much as 470 times. This would not be the case if there was competition between the M^+ and MO^+ ion formation; the observation rather suggests that addition of small amount of oxygen to the ICP can improve its atomization and ionization capabilities. The likely reason for this sensitivity enhancement is, similar to the addition of other molecular gasses, such as N_2 or H_2 , which improve heat transfer between the gas and sample aerosol. This is in accord with the computer simulations of the

1
2
3 addition of O₂ to the nebulizer gas reported by Cai et al. [55] that resulted in an
4 increase of plasma temperature.
5
6
7
8

9 **Concluding remarks**

10
11
12 The experimental data from this study show that even a small amount of oxygen
13 present in the ambient gas during the ablation of zircon can have pronounced
14 effects on the elemental fractionation of Si/Zr and Pb/U. This points to the
15 importance of maintaining constant and preferably low levels of ICP gas
16 impurities, such as O₂, during the ablation, and use of well maintained ablation
17 systems that are fully flushed and sealed against the atmosphere, as well as the
18 importance of close matrix-matching between standards and unknown samples.
19 Since the goal of the geoanalytical community is to reduce the present-day 2%
20 inter-laboratory bias [56] of U-Pb zircon dating by laser ablation ICP-MS to, or
21 below 1%, it is important that monitoring oxygen level and maintaining a
22 constant value during an analysis session becomes part of the laboratory routine.
23
24
25
26
27
28
29
30
31

32 The benefits of signal enhancement from the addition of O₂ to the He
33 sample carrier gas remain to be fully evaluated, and require long-term data sets
34 obtained by analysis of a variety of zircon compositions using a range of LA ICP-
35 MS instruments and operating conditions. The present study shows, however,
36 that maintaining a constant level of O₂ throughout the ablation cell and over an
37 analytical session is a pre-requisite to further improvement in U-Pb age
38 repeatability.
39
40
41
42
43
44
45
46
47
48
49
50
51
52
53
54
55
56
57
58
59
60

Acknowledgements

This study benefited from discussions with Henry Longerich while on a research visit to the Geological Survey of Canada. Comments by two anonymous reviewers helped to improve the quality of the manuscript. The authors acknowledge support received from the Czech Science Foundation (project P210/12/2114) and the GSC.

References

- 1 R. Feng, N. Machado and J. Ludden, *Geochim. Cosmochim. Acta*, 1993, **57**, 3479-3486.
- 2 B.J. Fryer, S.E. Jackson and H.P. Longerich, *Chem. Geol.*, 1993, **109**, 1-8.
- 3 T. Hirata and R.W. Nesbitt, *Geochim. Cosmochim. Acta*, 1995, **59**, 2491-2500.
- 4 S.E. Jackson, H.P. Longerich, I. Horn and G.R. Dunning, R., *J. Conf. Abstr.*, 1996, **1**, 283.
- 5 J.M. Hanchar and P.W.O. Hoskin (eds), *Zircon. Rev. Mineral. Geochem.*, 2003, **53**, 500 pp.
- 6 H.R. Kuhn and D. Günther, *Anal. Chem.*, 2003, **75**, 747-753.
- 7 M. Guilong and D. Günther, *J. Anal. At. Spectrom.*, 2002, **17**, 831-837.
- 8 J. Kosler, M. Wiedenbeck, R. Wirth, J. Hovorka, P. Sylvester and J. Mikova, *J. Anal. At. Spectrom.*, 2005, **20**, 402-409.
- 9 L.P. Black et al., *Chem. Geol.*, 2004, **205**, 115-140.
- 10 C.M. Allen and I.H. Campbell, *Chem. Geol.*, 2012, **332-333**, 157-165.
- 11 E. Kooijman, J. Berndt and K. Mezger, *Eur. J. Mineral.*, 2012, **24**, 5-21.
- 12 W. C. Butterman and W. R. Foster, *Am. Mineral.*, 1967, **52**, 880-885.
- 13 K.M. Ansdell and T.K. Kyser, *Am. Mineral.*, 1993, **78**, 36-41.
- 14 H. J. Chapman and J. C. Roddick, *Earth Planet. Sci. Lett.*, 1994, **121**, 601-611.
- 15 L. M. Heaman and A. N. LeCheminant, *Chem. Geol.*, 1993, **110**, 95-126.
- 16 J. Kosler, *Mineral. Assoc. Can. Short Course Series*, 2012, **42**, 185-202.
- 17 S. M. Eggins, L. P. J. Kinsley and J. M. G. Shelley, *Appl. Surf. Sci.*, 1998, **129**, 278-286.
- 18 A.J.G. Mank and P.R.D. Mason, *J. Anal. At. Spectrom.*, 1999, **14**, 1143-1153.
- 19 R.R. Parrish et al., *J. Conf. Abstr.*, 1999, **4**, 799.
- 20 J. Košler, *Mineral. Assoc. Can. Short Course Series*, 2008, **40**, 79-92.
- 21 J. Koch, M. Wälle, J. Pisonero and D. Günther, *J. Anal. At. Spectrom.*, 2006, **21**, 932-940.
- 22 I. Horn and F. von Blanckenburg, *Spectrochim. Acta B*, 2007, **62**, 410-422.
- 23 M. Guilong, I. Horn and D. Günther, *J. Anal. At. Spectrom.*, 2003, **18**, 1224-1230.
- 24 I. Horn, R.L. Rudnick and W.F. McDonough, *Chem. Geol.*, 2000, **167**, 405-425.
- 25 J. Košler, H. Fönneland, P. Sylvester, M. Tubrett and R.B. Pedersen, *Chem. Geol.*, 2002, **182**, 605-618.

- 1
2
3 26 C. Paton, J.D. Woodhead, J.C. Hellstrom, J.M. Hergt, A. Greig and R. Maas, *Geochem., Geophys., Geosyst.*, 2010, **11**, Q0AA06.
- 4
5 27 C. Paton, J.C. Hellstrom, P.B. Bence, J.D. Woodhead and J.M. Hergt, *J. Anal. At.*
6 *Spectrom.*, 2011, **26**, 2508-2518.
- 7
8 28 S.E. Jackson, *Geochim. Cosmochim. Acta*, 2009, **73**, A579.
- 9
10 29 B.K. Kuhn, K. Birmaum, Y. Luo and D. Günther, *J. Anal. At. Spectrom.*, 2010, **25**,
11 21-27.
- 12
13 30 I. Horn, M. Guillong and D. Günther, *Appl. Surf. Sci.*, 2001, **182**, 91-102.
- 14
15 31 D. Günther and C.A. Heinrich, *J. Anal. At. Spectrom.*, 1999, **14**, 1369-1374.
- 16
17 32 C.M. Petibon, H.P. Longerich, I. Horn and M.N. Tubrett, *Appl. Spectroscopy*,
18 **56**, 658-664.
- 19
20 33 T. Hirata, *Anal. Chem.* 2003, **75**, 228-233.
- 21
22 34 J. Kosler, H.P. Longerich and M.N. Tubrett, *Anal. Bioanal. Chem.*, 2002, **374**,
23 251-254.
- 24
25 35 K. Nishiguchi, K. Utani and E. Fujimori, *J. Anal. At. Spectrom.*, 2008, **23**, 1125-
26 1129.
- 27
28 36 R. Kovacs, K. Nishiguchi, K. Utani and D. Günther, *J. Anal. At. Spectrom.*, 2010,
29 **25**, 142-147.
- 30
31 37 S. F. Durrant, *Fresenius' J. Anal. Chem.*, 1993, **347**, 389-392.
- 32
33 38 N.N. Sesi, A. MacKenzie, K.E. Shanks, P. Yang, G.M. Hieftjie, *Spectrochim. Acta*
34 *Part B*, 1994, **49**, 1259-1282.
- 35
36 39 S.M. Burchell, Investigations of mixed-gas plasmas using a sheathing device
37 for ICP-MS, 2000, *MSc thesis Queen's University Kingston*, 161 pp.
- 38
39 40 M. Guillong and C.A. Heinrich, *J. Anal. At. Spectrom.*, 2007, **22**, 1488-1494.
- 40
41 41 S.F. Durrant, *Fresenius' J. Anal. Chem.*, 1994, **349**, 768-771.
- 42
43 42 S. Greenfield, I.L. Jones, H. McGreachin and P.B. Smith, *Anal. Chim. Acta*, 1975,
44 **74**, 225-245.
- 45
46 43 Z. Hu, S. Gao, Y. Liu, S. Hu, H. Chen, H. Yuan, *J. Anal. At. Spectrom.* 2008, **23**
47 1093-1101.
- 48
49 44 R. C. Hutton, *J. Anal. At. Spectrom.*, 1986, **1**, 259-263.
- 50
51 45 M.J. van de Sande, P. van Eck, A. Sola, A. Gamero and J.J.A.M. van der Mullen,
52 *Spectrochim. Acta B*, 2003, **58**, 457-467.
- 53
54 46 S.E. Jackson, N.J. Pearson, W.L. Griffin and E.A. Belousova, *Chem. Geol.*, 2004,
55 **211**, 47-69.
- 56
57 47 L.P. Black and B.L. Gulson, B.L., *BMR J. Austral. Geol. Geophys.*, 1978, **3**, 227-
58 232.
- 59
60 48 P.J. Sylvester and M. Ghaderi, *Chem. Geol.*, 1997, **141**, 49-65.
- 49 R. Wirth, *Eur. J. Mineral.*, 2004, **16**, 863-876.
- 50 R. Wirth, *Chem. Geol.*, 2009, **261**, 217-229.
- 51 A.H. Wang, W.Y. Wang, C.S. Xie, W.L. Song and D.W. Zeng, *Appl. Surf. Sci.*,
2004, **227**, 104-113.
- 52 C.E. Curtis and H.G. Sowman, *J. Am. Chem. Soc.*, 1953, **36**, 190-198.
- 53 S. Ellsworth, A. Navrotsky and R.C. Ewing, *Phys. Chem. Minerals*, 1994, **21**,
140-149.
- 54 I. Farnan and E.K.H. Salje, *J. Appl. Phys.*, 2001, **89**, 2084-2090.
- 55 M. Cai, D.A. Haydar, A. Montaser and J. Mostaghimi, *Spectrochim. Acta B*,
1997, **52**, 369-386.
- 56 J. Kosler et al., *Geost. Geoanal. Res.*, 2013, **37**, 243-259.

Figure captions

Figure 1

Experimental setup for laser ablation sampling of zircon at variable oxygen concentration in the He sample carrier gas.

Figure 2

Schematics of sample preparation for the FIB/TEM study. A. sectioning the zircon grain, B. laser ablation along the joint, C. separation of the two parts of the sample, D. sampling the wall and bottom of the ablation pit by focused ion beam (the laser pit was filled with epoxy and coated with protective Pt layer).

Figure 3

The effects of oxygen in the He sample carrier gas on the measured signal intensities of A. ^{29}Si and ^{96}Zr , B. ^{206}Pb and ^{238}U and C. ^{248}ThO and ^{254}UO . Proportion of ^{248}ThO and ^{254}UO calculated as $\text{MO}^+/\text{M}^+ \times 100$ [%] is shown in D.

Figure 4

The effects of oxygen in the He sample carrier gas on A. the measured signal intensity ratios of $^{29}\text{Si}/^{96}\text{Zr}$ and $^{206}\text{Pb}/^{238}\text{U}$. Diagrams B. and C. show the separate effects of oxygen concentration in the He sample carrier gas on the slope and intercept [48] of the elemental fractionation trends of $^{29}\text{Si}/^{96}\text{Zr}$ and $^{206}\text{Pb}/^{238}\text{U}$, respectively. Uncertainties on the intercept are 1 sigma.

Figure 5

Secondary electron images of the ablation pits produced in the Mud Tank zircon sample at different concentrations of oxygen in the He sample carrier gas. Figures E. and F. show details of the wall deposit with cooling cracks and corrugated surface.

Figure 6

Transmission electron microscopy images of the FIB foils cut from the laser ablation craters in the Mud Tank zircon produced at different concentrations of oxygen in the He sample carrier gas. A. to D. are high-angle annular dark field (HAADF) images of the FIB foils from the crater walls, E. shows detail of the wall structure in C. F. and G. are bright field (BF) images of the interface between the crater walls and the wall deposits produced with pure He sample carrier gas, H. and I. are HAADF images from the bottoms of the laser craters. Since the structure and composition of the bottom part of the craters does not change with the oxygen concentration, only two images are shown.

Text for graphical abstract:

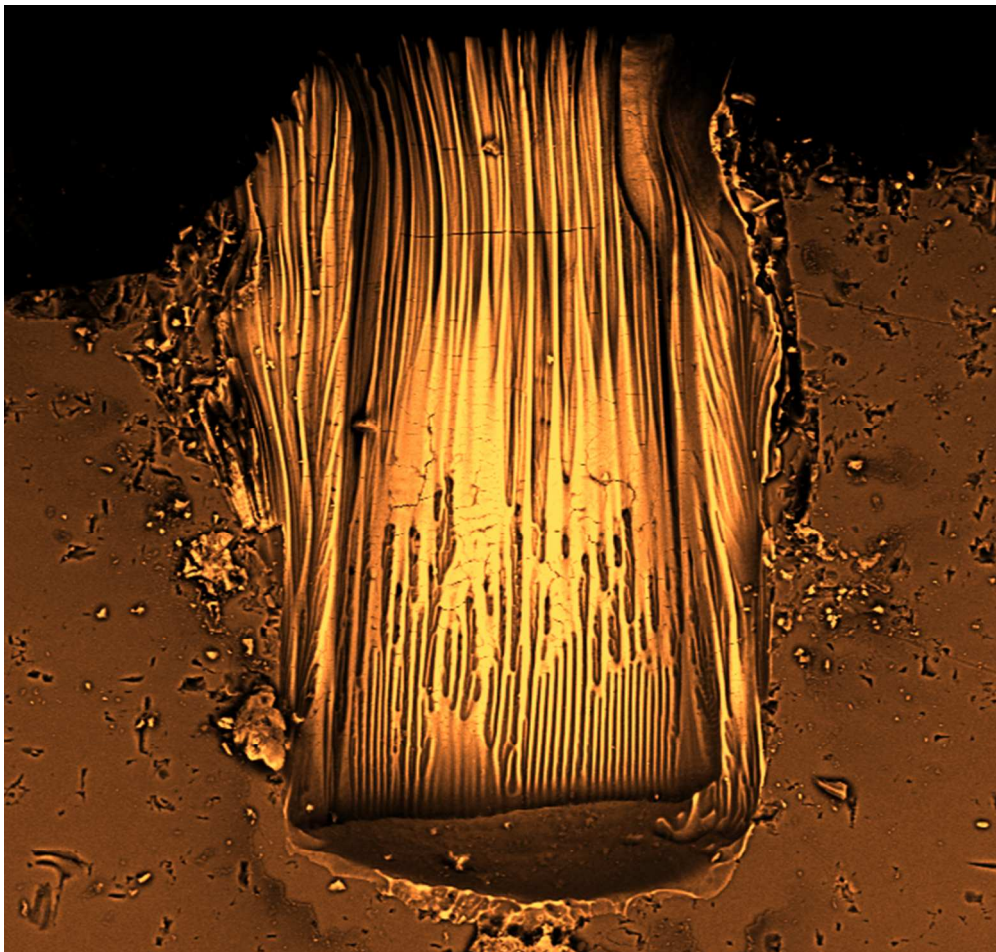
Presence of oxygen during U-Th-Pb LA ICP-MS analysis of zircon controls the laser-induced elemental fractionation and ICP-MS sensitivity.

Description of the image:

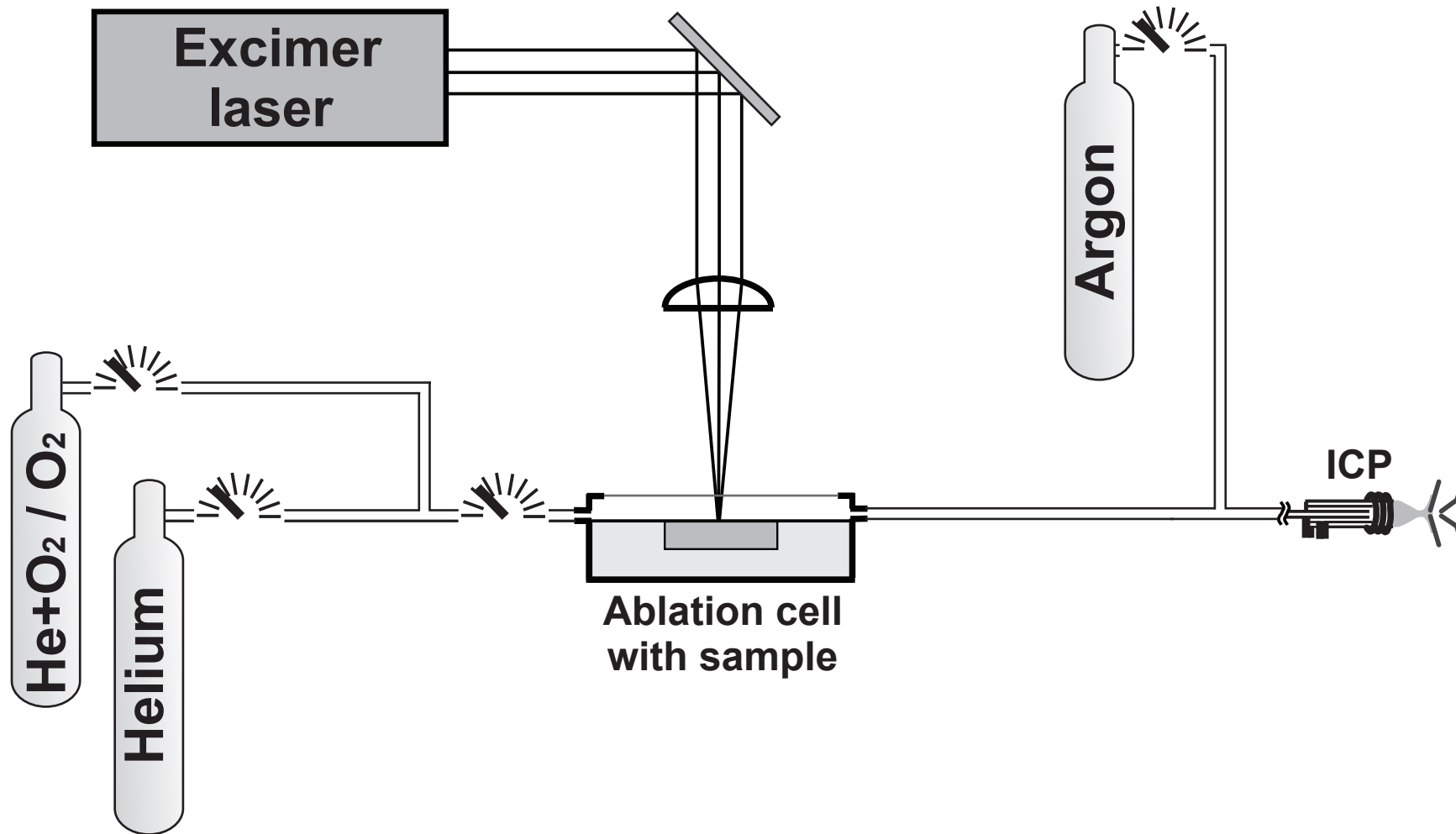
Secondary electron image shows side view of a laser ablation crater produced in the Mud Tank zircon sample. The crater dimensions are ca. 85 μm (width) x 150 μm (depth). The inner wall of the crater is covered by a deposit of ablation products (ZrO_2 and SiO_2) with cooling cracks and corrugated surface, the bottom of the crater is covered by ca. 0.18 μm thick layer of ZrSiO_4 glass.

1
2
3
4
5
6
7
8
9
10
11
12
13
14
15
16
17
18
19
20
21
22
23
24
25
26
27
28
29
30
31
32
33
34
35
36
37
38
39
40
41
42
43
44
45
46
47
48
49
50
51
52
53
54
55
56
57
58
59
60

1
2
3
4
5
6
7
8
9
10
11
12
13
14
15
16
17
18
19
20
21
22
23
24
25
26
27
28
29
30
31
32
33
34
35
36
37
38
39
40
41
42
43
44
45
46
47
48
49
50
51
52
53
54
55
56
57
58
59
60



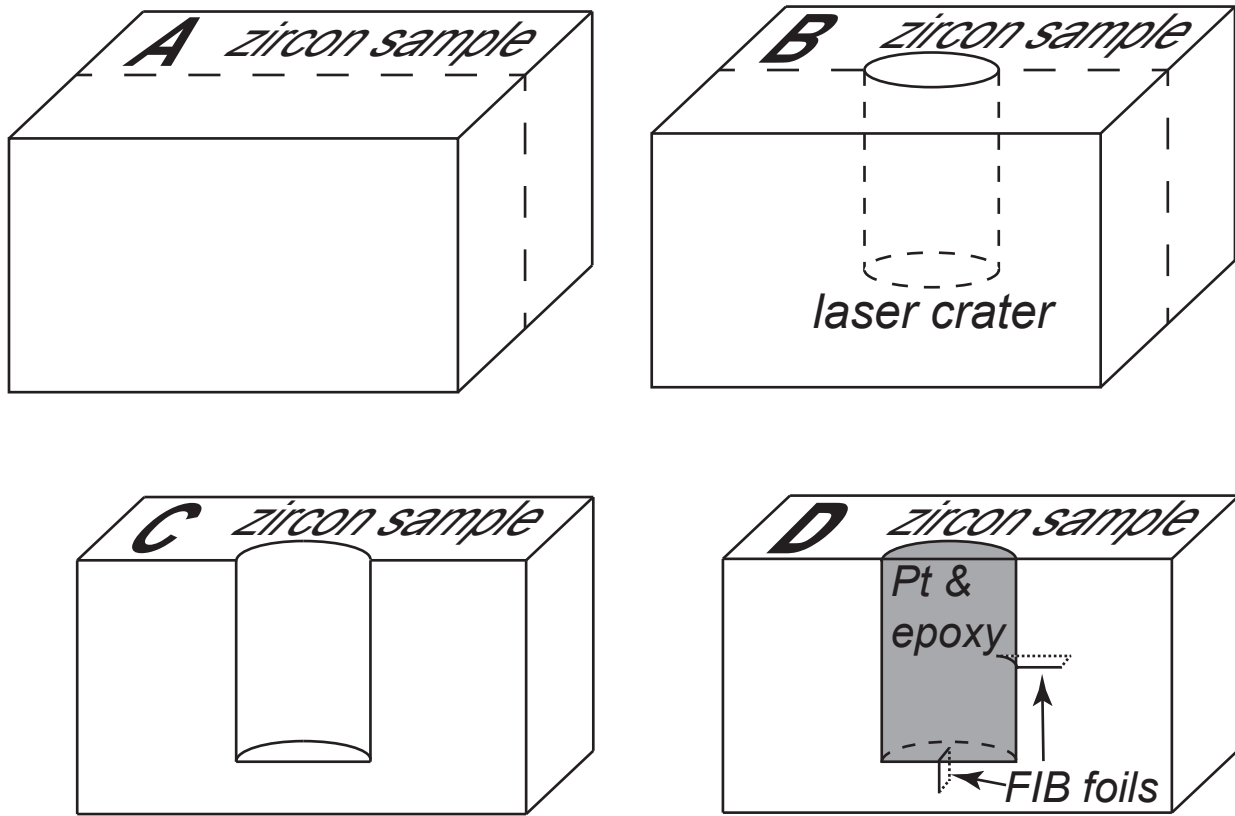
17526x16637mm (1 x 1 DPI)



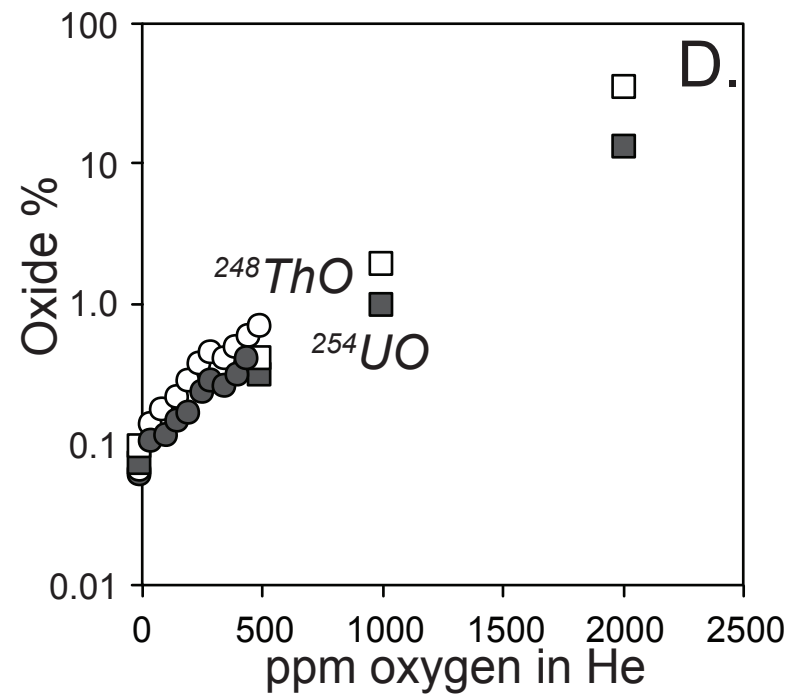
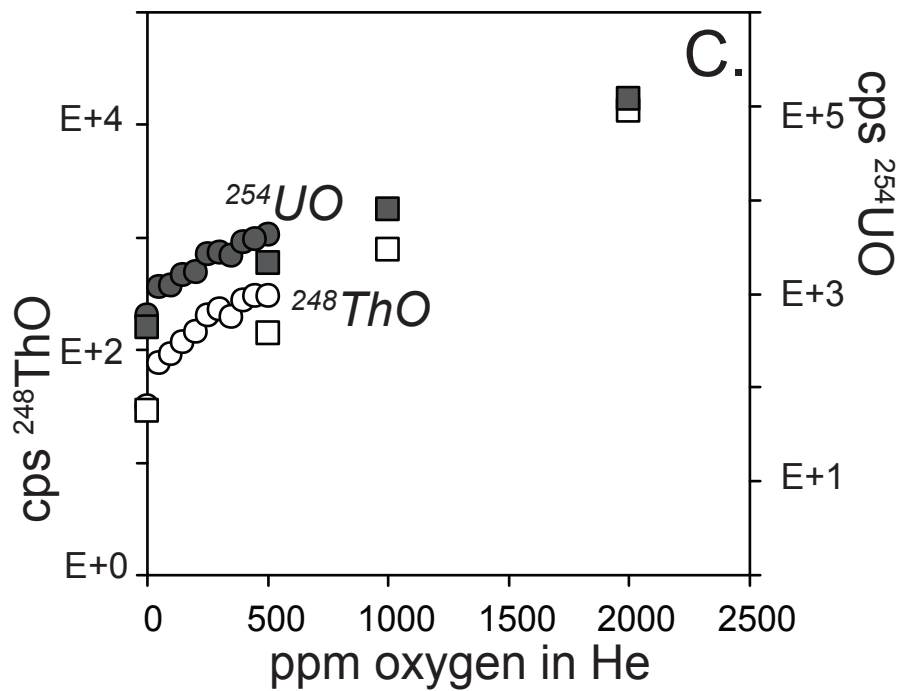
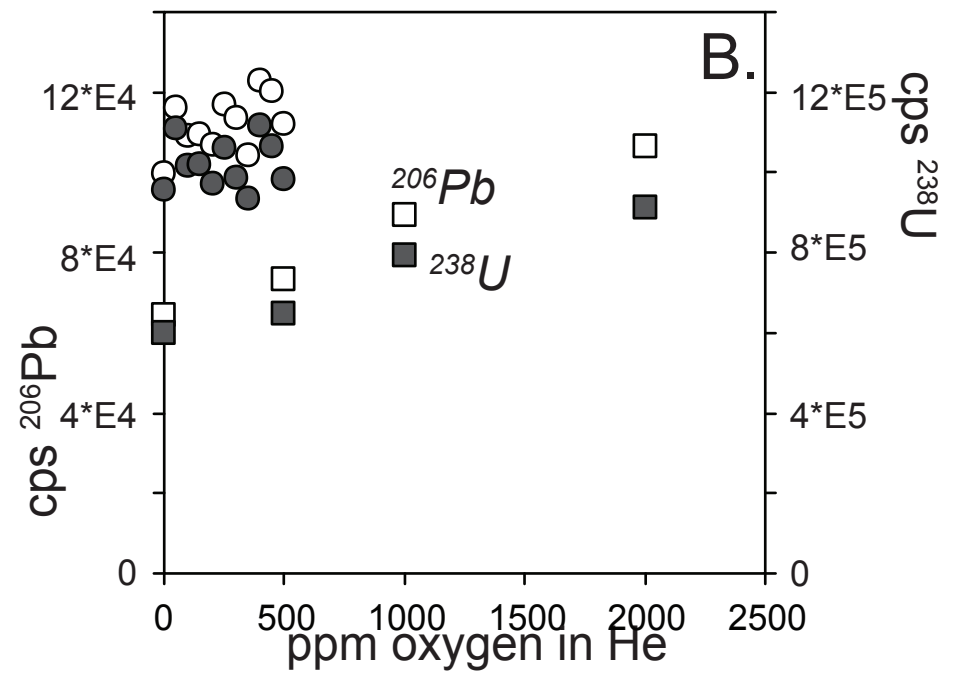
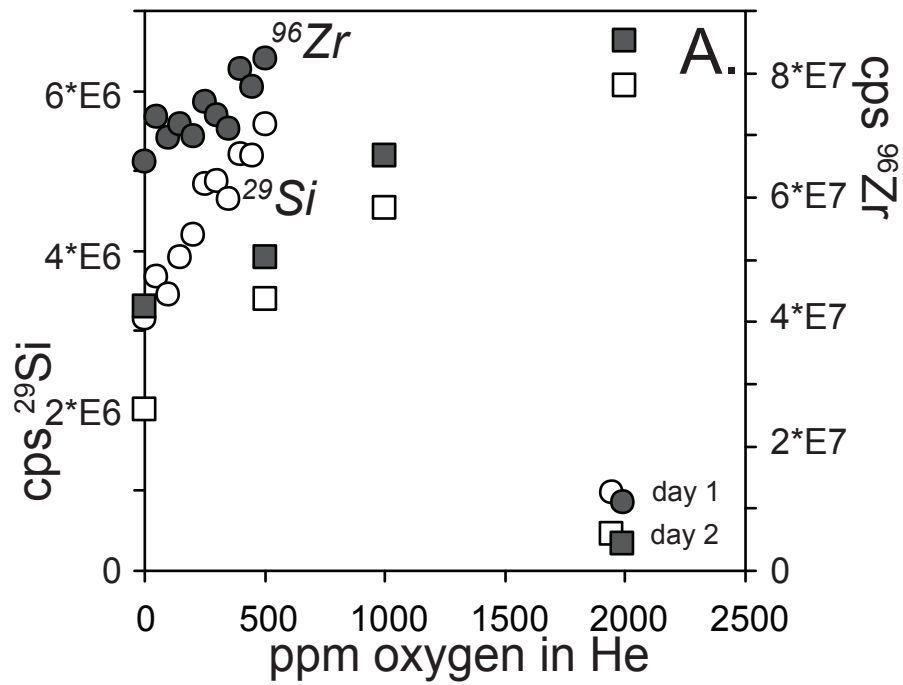
Kosler et al., Figure 1

Journal of Analytical Atomic Spectrometry Accepted Manuscript

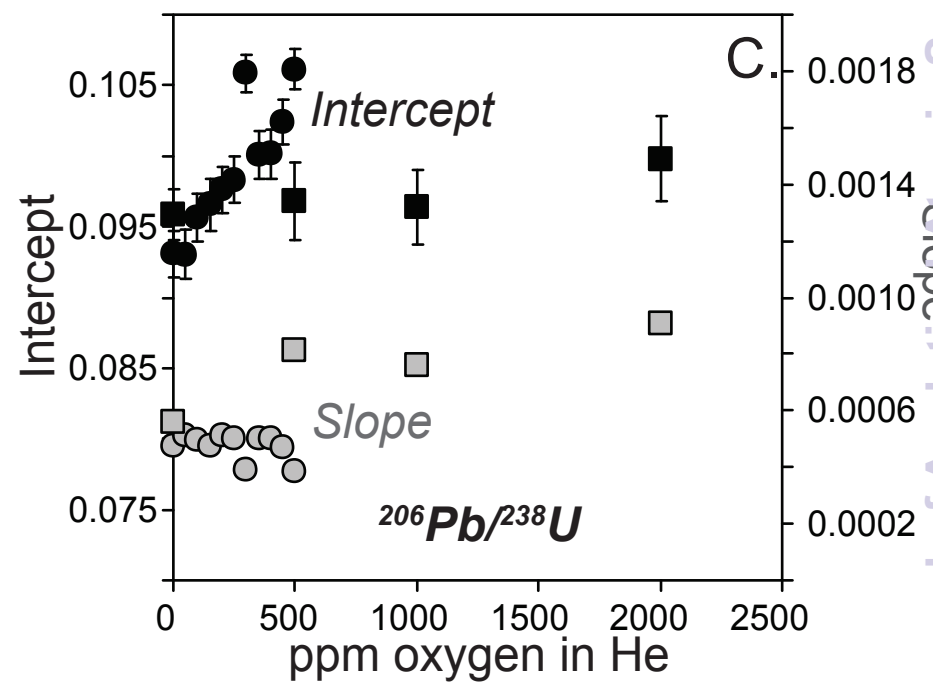
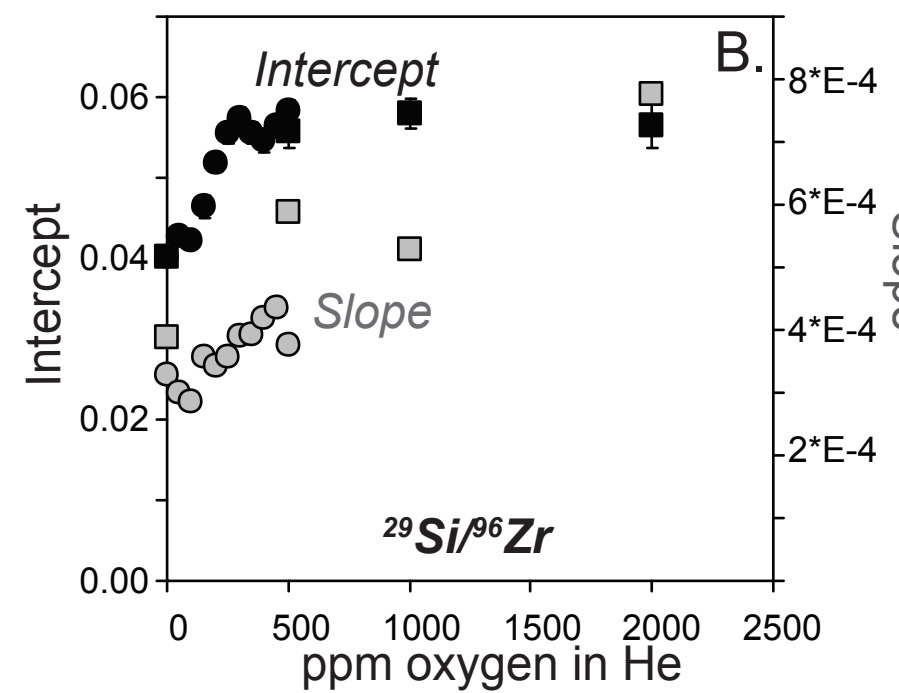
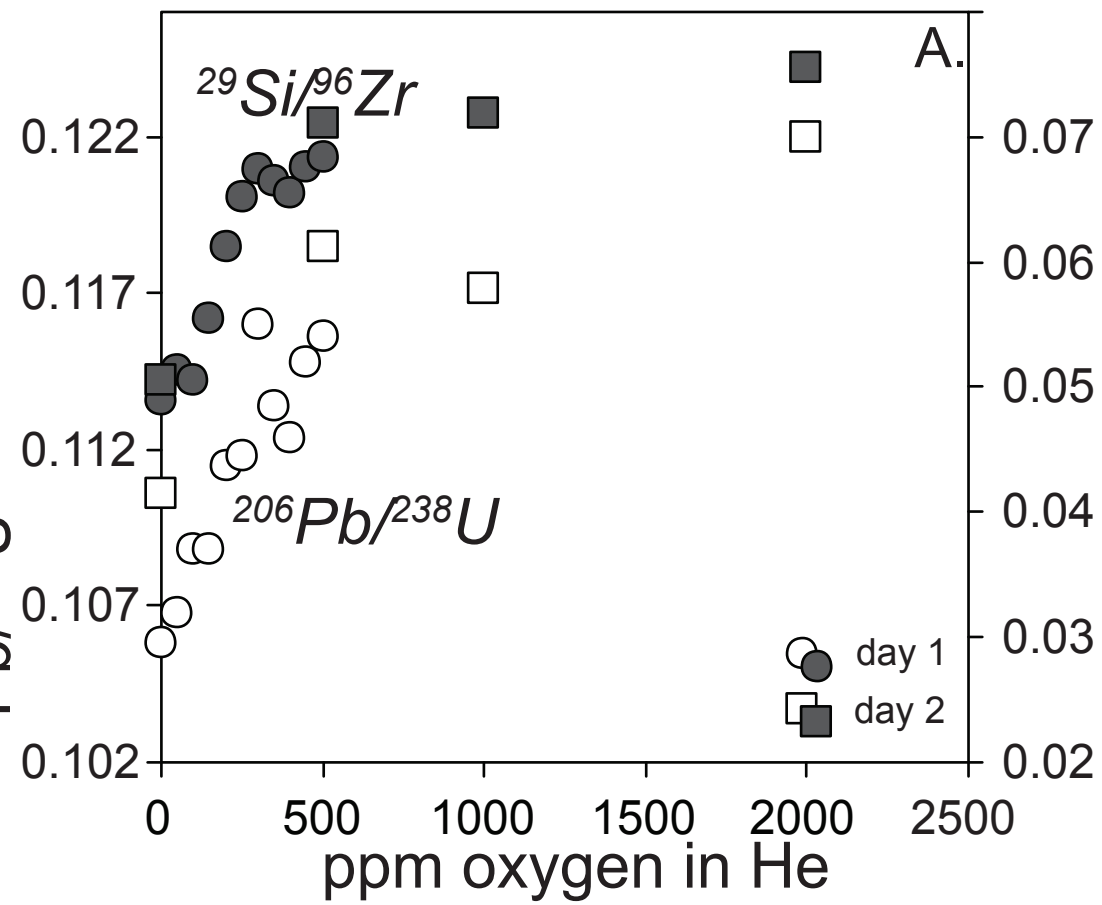
1
2
3
4
5
6
7
8
9
10
11
12
13
14
15
16
17
18
19
20
21
22
23
24
25
26
27
28
29
30
31
32
33
34
35
36
37
38
39
40
41
42
43
44
45
46
47
48
49



1
2
3
4
5
6
7
8
9
10
11
12
13
14
15
16
17
18
19
20
21
22
23
24
25
26
27
28
29
30
31
32
33
34
35
36
37
38
39
40
41
42
43
44
45
46
47
48
49
50
51
52
53
54
55
56
57
58
59
60



1
2
3
4
5
6
7
8
9
10
11
12
13
14
15
16
17
18
19
20
21
22
23
24
25
26
27
28
29
30
31
32
33
34
35
36
37
38
39
40
41
42
43
44
45
46
47



Kosler et al., Figure 4

Journal of Analytical Atomic Spectrometry Accepted Manuscript

